Observation of dynamic liquid water transport in the microporous layer and gas diffusion layer of an operating PEM fuel cell by high-resolution soft X-ray radiography

Phengxay Deevanhxay [a,*], Takashi Sasabe [b], Shohji Tsushima [a], Shuichiro Hirai [a]

[a] Department of Mechanical and Control Engineering, Tokyo Institute of Technology, 2-12-1 Ookayama, Meguro-ku, Tokyo 152-8552, Japan
[b] Institute of Fluid Science, Tohoku University, 2-1-1, Katahira, Aoba-ku, Sendai, Miyagi 980-8577, Japan

HIGHLIGHTS

► In-situ observation of liquid water transport in a PEMFC's MPL and GDL is performed.
► High-resolution soft X-ray radiography is used to observe the liquid water.
► The liquid water in the MPL and GDL increases with increasing in current density.
► The liquid water in the MPL is low near the CL and higher toward the GDL side.
► The dynamic liquid water transport from the MPL cracks to the GDL pores is observed.

ARTICLE INFO

ABSTRACT

In-situ observation of liquid water transport in the microporous layer (MPL) and gas diffusion layer (GDL) of an operating proton exchange membrane fuel cell (PEMFC) was performed using high-resolution soft X-ray radiography. The amount of liquid water accumulated in the MPL and GDL increases with increasing in current density. The amount of liquid water in the MPL is low near the catalyst layer and higher toward the GDL side. The liquid water is transported to the GDL mainly through the cracks in the MPL. The dynamic liquid water transport from the cracks in the MPL to the interconnected pores in the GDL was observed.

1. Introduction

Appropriate water management is critical for achieving high power density and increased robustness in proton exchange membrane fuel cells (PEMFCs) [1–3]. For the purpose of water management, the implementation of a hydrophobic polymer in the gas diffusion layer (GDL) and the addition of a microporous layer (MPL) to the GDL side facing the catalyst layer (CL) have been studied in a number of theoretical and experimental investigations [4–10]. It is generally accepted that adding an MPL to the GDL helps improve the performance of PEMFC. The MPL has been considered to provide better electrical and thermal contact between the CL and the GDL; and to improve the mass transport at high current density. It is believed that the MPL alters the liquid water distribution in the GDL. However, liquid water transport in the MPL is still not fully understood.

Several models [5–7] predict that the MPL should acts as a capillary barrier and forces the water to permeate from the cathode to the anode. Spernjak et al. performed an experimental investigation of liquid water formation and transport in a transparent PEMFC [9]. They found that the liquid water appeared in the anode channels only when an MPL was used on the cathode side, suggesting that the MPL functions as a capillary barrier. However, Ge and Wang reported that the appearance of water in the anode resulted from condensation of water on the channel walls and that the condensed water did not come from the cathode through the

* Corresponding author. Tel./fax: +81 3 5734 3554.
  E-mail address: deevanhxay.p.aa@m.titech.ac.jp (P. Deevanhxay).

membrane [10]. Atiyeh et al. conducted an overall water balance measurement and found that the presence of the MPL did not affect the net water drag coefficient [11], indicating that the improvement in fuel cell performance due to the presence of the MPL is not associated with overall water drag. A direct analysis of water in the cathode CL, GDL, and flow field after operation was performed by Nakajima et al. [12]. They found that the MPL reduced the water accumulation in the CL. In addition, Kong et al. reported that the macro-pores in the MPL enhanced the performance of the PEMFC [13], implying that the macro-pores in the MPL may be effective in removing liquid water from the CL. Recently, Gostick et al. performed an ex-situ experiment to study the saturation and capillary pressure of GDLs with and without an MPL [14]. They reported that the GDL saturation at water breakthrough was drastically reduced by the presence of an MPL, indicating that the MPL restricts the number of entry points for water to get into the GDL. Lu et al. observed that no dynamic change in the breakthrough location was found when GDL with an MPL was used [15], suggesting that the MPL stabilized the water paths in the GDL.

In-situ observation is essential for a better understanding of liquid water in PEMFC. Several techniques have been developed for visualization of liquid water inside the membrane electrode assembly (MEA) [3,16]. Among them, neutron radiography is a well-established technique for studying the water distribution in the MEA. Hickner et al. demonstrated that a region with low water content exists near the MPL/GDL boundary and that there is a region with high water content at the GDL/gas flow channel boundary [17]. Several investigations have found that the MPL increased the water content in the anode, which supports the back diffusion hypothesis [17–21]. Boillat et al. measured the changes in the water distribution in a GDL with an MPL by using neutron radiography with a resolution of 20 μm and exposure times of 10 s [22]. However, the present spatial resolution of neutron radiography is not sufficient to gain insight into the water transport pathways on the scale of the pore in the GDL. For this purpose, X-ray radiography has been a potential candidate for observing liquid water at high spatial and temporal resolution [23–26]. Manke et al. used synchrotron X-ray radiography with a spatial resolution of 3 μm to study water transport in a felt GDL [23]. They observed an "eruptive transport" mechanism, which they suggested to be the quick ejection of droplets from the GDL under the rib into the channels. Markötter et al. found a possible water transport pathway by combining in-situ radiography with quasi-in-situ tomography technique [26]. In order to visualize liquid water at high spatial and temporal resolution, our research group developed soft X-ray radiography technique with a maximum resolution of 0.5 μm [27]. We succeeded in visualizing the liquid water transport behavior in different types of GDLs [28,29] and in the micro-cracks of the MPL on the woven carbon cloth [30]; and visualizing liquid water distribution in the cathode catalyst layer [31].

In this study, we aim to investigate the dynamic water accumulation and transport in cathode MPL and GDL at high spatial and temporal resolution. The amount of liquid water accumulated in the MPL and GDL increased with increasing current density. The liquid water generated from the reaction was transported to the GDL through the cracks in the MPL. The amount of liquid water in the MPL was low near the CL, but became higher toward the GDL side under the rib. The liquid water transport through the cracks of the MPL to the interconnected pores in the GDL was visualized.

2. Experimental

Fig. 1 shows the cell structure used in this study. A CL with a loading of Pt of 0.22 mg cm^{-2} was decaled on to perfluorinated sulfonic acid (PFSA) membrane (Nafion® NRE-211, 2 pieces, 50 μm
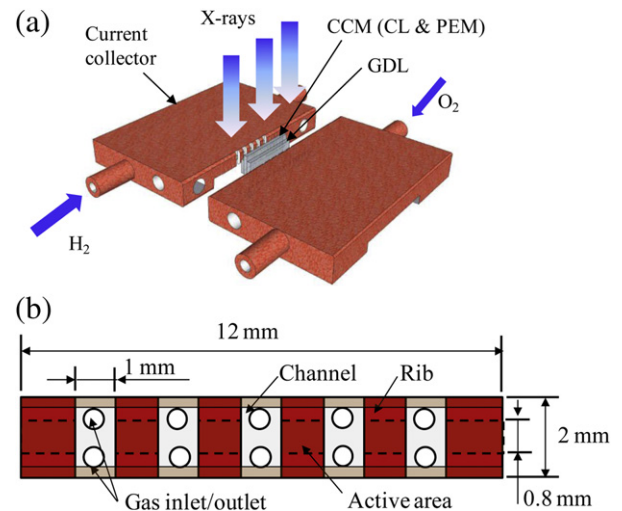

Fig. 1. (a) Schematic diagram of the cell for cross-sectional imaging, and (b) flow field configuration.

thick) by hot-pressing to make the catalyst-coated membrane (CCM). The active area was 0.1 cm^2 (0.8 × 12 mm^2). SIGRACET®24BC GDLs with MPLs (SGL Carbon, 235 μm thick) were used as the anode and cathode GDLs. The membranes were fold to cover the top and bottom sides of the CL and GDL, and adhered to the current collectors by Kapton® tape to seal the gases. This observation cell was designed to allow the soft X-ray to pass through the MEA. Although the cell structure was slightly different from that of conventional one (large cell), the characteristic of the cell was similar to that of conventional one regarding the cell performance and impedance arcs those represent the resistances of each process in fuel cell [31]. Therefore, the influence of structure difference on the liquid water transport at micro scale can be negligible. For the operating conditions, hydrogen and oxygen gases with relative humidity of 60% were used at a flow rate of 100 sccm. The cell was tested at current densities of 0.20–0.60 A cm^{-2} at 30 °C by a fuel cell test system (NF Corp.).

The visualization was performed by using a laboratory-base soft X-ray microscope system [27–31]. A vanadium thin-film was used as the target material for generating soft X-rays, and the X-ray tube voltage was set at 15 kV. Alignment was performed before observing the fuel cell by using a microchart (JIMA RT RC-02), with which a line pitch of 1.5 μm could be discriminated at the cell position. The cell was carefully fixed on a computer-controlled four-axis stage, that was able to move in the X, Y, and Z directions with a resolution of 1 μm and rotate around the Z-axis. The stage allowed accurate alignment of the cell with the X-ray beam. The surface of the cell was adjusted to be perpendicular to the X-ray beam. The center of the MPL was aligned with the center of the image reception area, which was along the beam axis. The images were captured by an imaging system comprised of 1024 × 1024 pixel electron multiplication charge-couple device (EM-CCD) camera with 16-bit depth (Hamamatsu photonic k.k.) and processing computer. All the images were taken at 1 frame per second (fps), and an image with 32 s of integration time was used to calculate the liquid water distribution. HCImage (Hamamatsu photonic k.k) and ImageJ (National institute of health) software were used for image processing. The liquid water thickness was calculated using a dry image and an image with liquid water as references. The porosities of the MPL and GDL were set to 0.35 and 0.84 [32], respectively.

3. Results and discussion

3.1. Effect of current density on water accumulation and transport in the cathode MPL and GDL

Fig. 2 shows soft X-ray radiograph of the MEA. Fig. 2(b) presents high magnification observed image of the rectangular area under the rib indicated in Fig. 2(a). Each layer of the MEA can be identified by attenuation differences due to their different chemical constituents and layer densities [29]. Fig. 3 shows the subtracted images derived from images taken under open-circuit voltage conditions (0.80 V) and images taken after different operating times, in order to represent the distribution of liquid water in the MPL and GDL as a function of operating time. The dynamic liquid water accumulation at 1 fps is shown in video clips 1, 2, and 3 for operation at 0.20 A cm^{-2} (0.41 V), 0.40 A cm^{-2} (0.25 V), and 0.60 A cm^{-2} (0.10 V) respectively. At a current density of 0.20 A cm^{-2} (Fig. 3(a)), only a small change was observed in the images, which indicates that almost no liquid water was present. On the other hand, when the current density was increased to 0.40, and 0.60 A cm^{-2} (Fig. 3(b) and (c)), accumulation of liquid water was observed in the MPL and GDL. A large amount of liquid water accumulated in the GDL, and small amount was observed in the MPL. There are areas with high amounts of liquid water in the MPL after power generation, implying that there are liquid water transport pathways in the MPL.

The video clip shows the subtracted images derived from images taken under open-circuit voltage conditions and images taken during operation. The light blue to brown color illustrated the liquid water. The images were taken at 1 fps. The yellow−brown lines at the interface of CL and MPL in cathode and anode could be caused by the membrane swelling during operation.

Supplementary material related to this article can be found online at http://dx.doi.org/10.1016/j.jpowsour.2012.11.140.

Fig. 4 shows the profiles of the average amount of liquid water across the cathode MPL and GDL as a function of operating time at each current density. There was almost no water observed at 0.20 A cm^{-2} (Fig. 4(a)), indicating that the generated water was mainly transported as vapor under this operating condition. When the current density was increased to 0.40 (Fig. 4(b)) and 0.60 A cm^{-2} (Fig. 4(c)), the amount of liquid water in the MPL and GDL increased as the operating time increased. There was more accumulated liquid water at 0.60 A cm^{-2} than at 0.40 A cm^{-2}. However, the liquid water did not change much after 150 s for the

operation at 0.60 A cm^{-2}, suggesting that the liquid water accumulation in GDL nearly reach the steady-state at 150 s and the liquid water under the rib is continuously removed to the channel. In the calculation of liquid water thickness in Fig. 4, we set the initial porosity of the MPL and GDL as 0.35 and 0.84 [32], although the porosity distribution may exist in MPL and GDL as recently reported by Fishman and Bazylak [33]. From this calculation, the through-plane liquid water saturations at 210 s of the operation at 0.60 A cm^{-2} are 0.03−0.13 in the MPL, and 0.14−0.40 in the GDL. Therefore, the average liquid water saturation in the MPL and GDL are 0.08 and 0.27, respectively. This result suggested that there is still enough voice space for gas diffusion at this operating condition.

In addition, there was also enhanced accumulation behavior of the liquid water in the GDL toward the rib side. This observation is similar to the water distribution obtained by neutron radiography [17,20−22]. However, the details of this water distribution have not been fully explained. It is well-known that liquid water moves from high water saturation regions to lower saturation regions through capillary-induced liquid water transport, as observed in GDLs without MPLs. In spite of this, the liquid water accumulation in the GDL with MPL shows reversed distribution. Phase-change due to temperature gradient, morphology, and interface property of porous media may play a role in this liquid water accumulation. Turhan et al. suggested that the phase-change-induced flow exists in the diffusion media and the capillary-induced flow dominates the removal of liquid water from the rib to channel in their experiment performed at 65 °C [21]. However, they also suggested that the MPL surface cracks and interface morphology have an important impact on liquid storage and distribution. In our experiment, the effect of phase-change could be small because the cell was operated at low temperature at 30 °C. For instance, the difference in saturation vapor pressure at 30 °C and 35 °C is only 1% (at 1 atm total pressure). Therefore, the morphology and the property of the MPL and GDL should have larger effect on the water transport. The observation of capillary-induced liquid water transport in GDLs without MPLs may be because the GDLs without MPLs have many entry points for liquid water and their porosity is relatively uniformed. However, the number of entry points is limited and the porosity is not uniform for GDLs with MPLs. There are cracks and holes in the MPLs [33], which could form liquid water transport pathways. The liquid water could be selectively transported to the GDL by a relatively larger path in the MPL. In
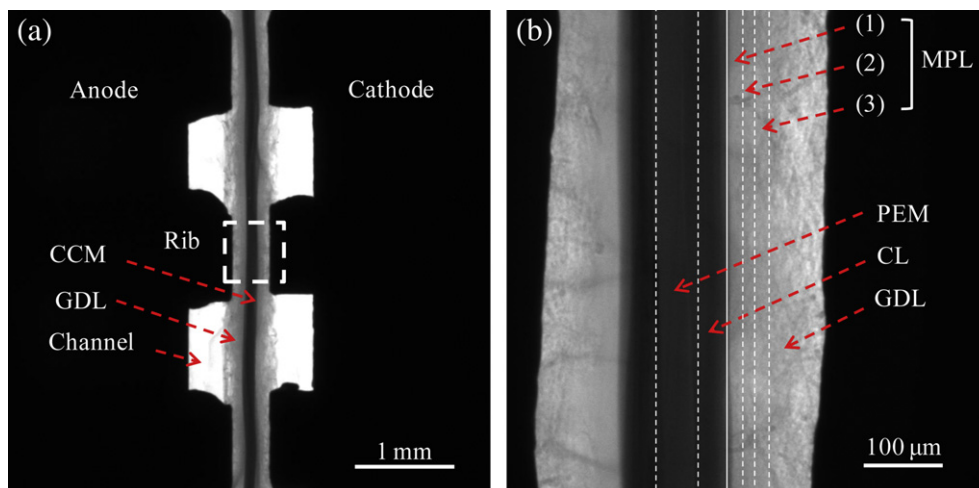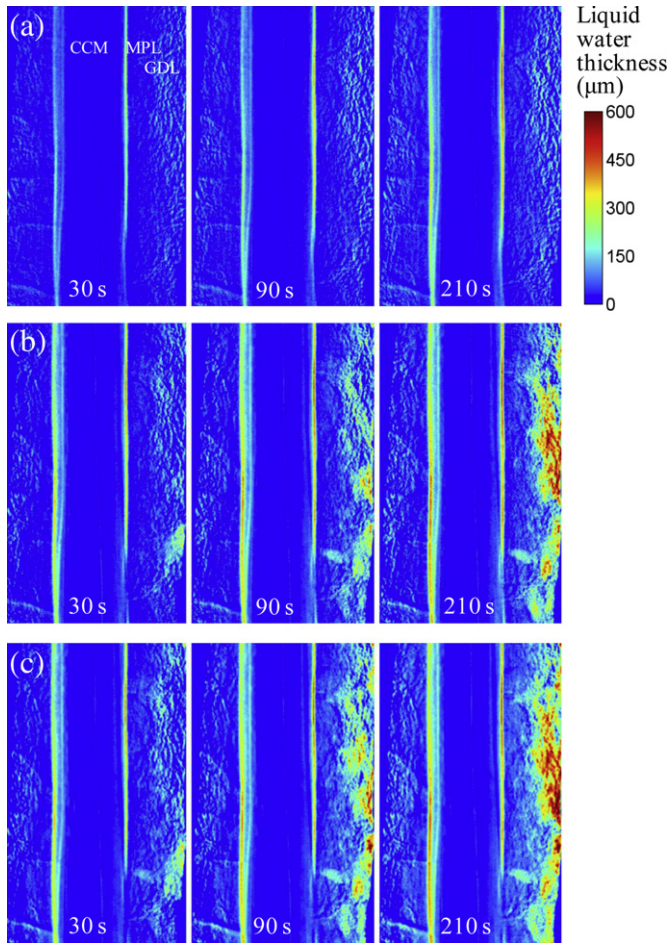

Fig. 2. Soft X-ray radiographs of the MEA: (a) radiograph at low magnification, and (b) radiograph of the selected area at high magnification. The numbers 1, 2, and 3 in the MPL region indicate the areas those were used to calculate the liquid water distribution along the MPL shown in Fig. 6(a).
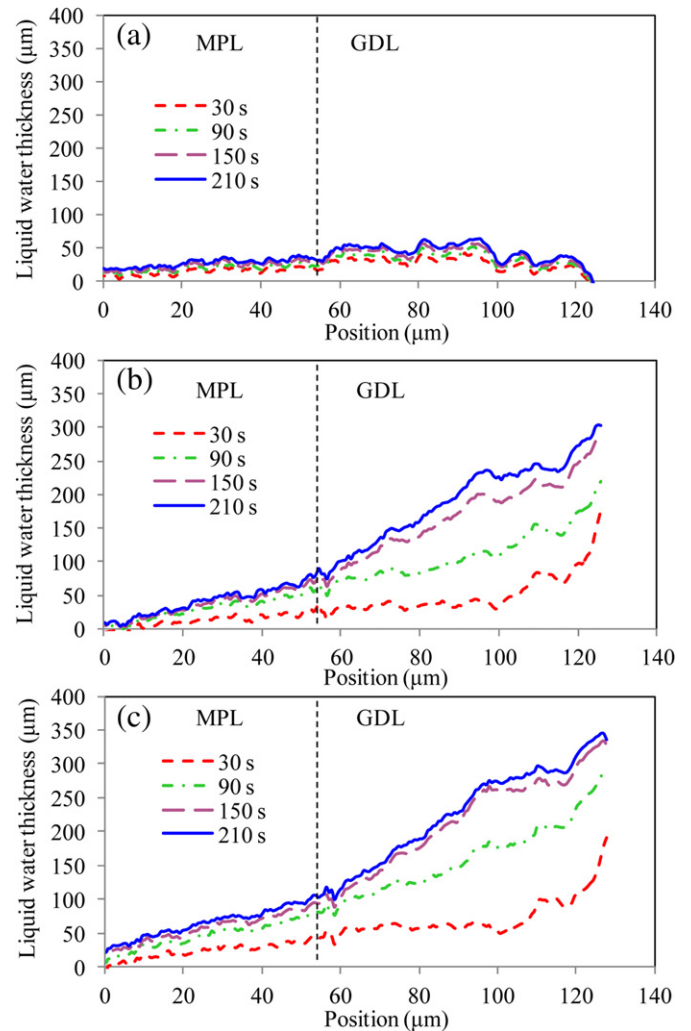
Fig. 3. Liquid water distribution at each current density: (a) 0.20 A cm^{-2}, (b) 0.40 A cm^{-2}, and (c) 0.60 A cm^{-2}.

Fig. 4. Average liquid water thickness in the MPL and GDL at (a) 0.20 A cm^{-2}, (b) 0.40 A cm^{-2}, and (c) 0.60 A cm^{-2}.

addition, the penetration of MPL's carbon black into the GDL could generate a non-uniform porosity distribution across the GDL and form pathways for liquid water transport in the GDL. The porosity of GDL with MPL could be low in MPL side and high toward the surface of GDL [33]. The inhomogeneous pathway in the MPL and the distribution of the porosity in a GDL with an MPL may be one reason for enhanced accumulation of liquid water toward the rib.

Fig. 5(a) shows the liquid water profiles in the MPL plane indicated in Fig. 2(b). The numbers 1, 2, and 3 represent the areas in the MPL used for the calculation. There are several high peaks in the water distribution in the MPL, indicating the liquid water transport pathways. Fig. 5(b) shows a scanning electron microscopy (SEM) image of the surface of the MPL after the visualization experiment. Several cracks with widths of 10–20 μm and lengths of 100–400 μm were observed on the surface of the MPL. These cracks corresponded well to the liquid water pathways observed by soft X-ray radiography in Fig. 5(a). It is obvious that the liquid water was transported through the cracks in the MPL and accumulated under the rib at high current density. It is important to emphasize that the generated water could be transported as a gas or as a liquid in the MEA, depending on the change in water vapor pressure due to water generated from the reaction. At low current density, the water is transported in the gas phase, since the amount water generated is small and the water vapor pressure could be lower than the saturated water vapor pressure. When the current density is increased, the water vapor pressure could exceed the saturated vapor pressure in the CL or in the interface between the CL and

MPL. Then, it could be transported as a liquid through the crack in the MPL. When we calculated the amount of liquid water present in the MPL at the beginning of operation, we noticed that approximately 10% of the total amount of water generated at 0.60 A cm^{-2} was transported in liquid form.

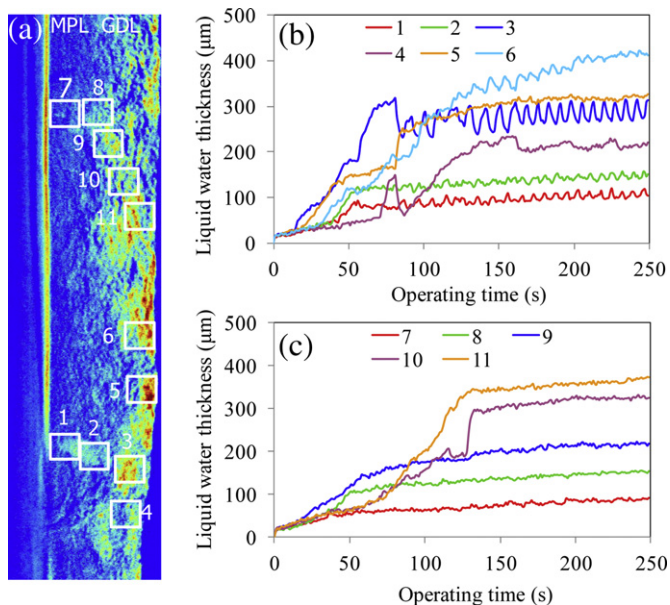### 3.2. Analysis of dynamic liquid water transport and its pathway in the MPL/GDL

Water is produced dynamically during power generation in PEMFC. The dynamic water accumulation could affect the reactant gas transport and reduce the performance of fuel cell, especially at high current density. Therefore, it is important to understand the dynamic liquid water transport in the MPL and GDL. We observed four main pathways of liquid water transport through the cracks in the MPL surface, as indicated in Fig. 5. We noticed that the cracks could be connected to the pores in the GDL. In order to see the dynamic liquid water transport and its pathways on the scale of the pores, we analyzed the local amount of liquid water at each location in the MPL and GDL as a function of operating time. Fig. 6(a) shows the locations used for the calculations in two liquid water transport pathways. Each square corresponds to an area of 35 × 35 μm^2. The changes in the amount of liquid water at each location under
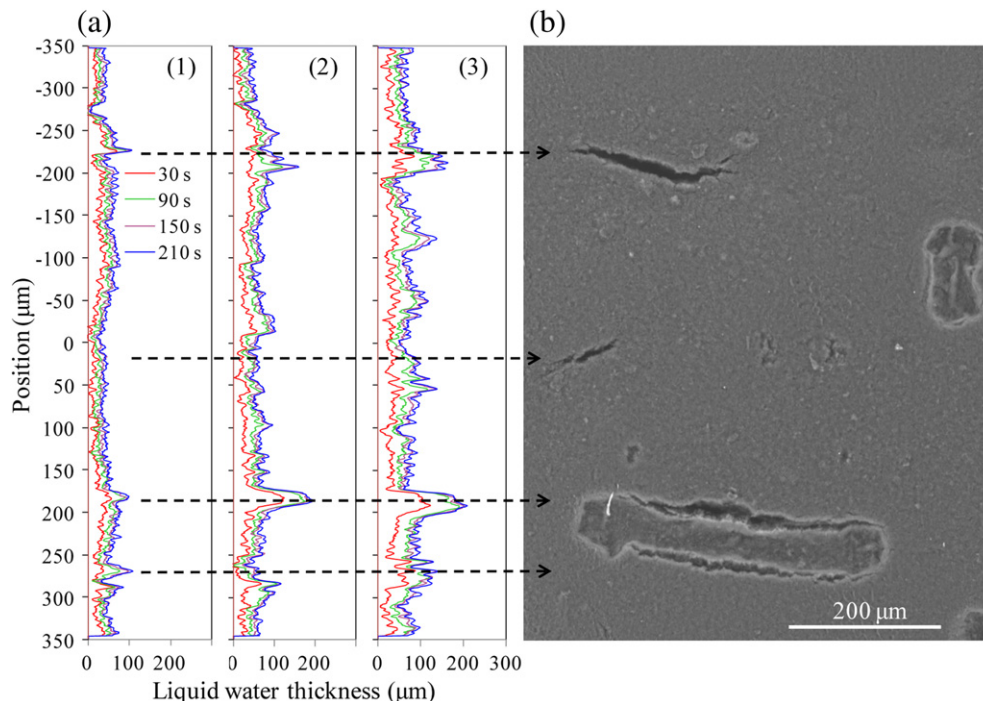
Fig. 5. (a) Average liquid water thickness in the MPL plane at 0.60 A cm^{-2} and (b) SEM image of the MPL surface. The numbers 1, 2, and 3 in the parenthesis represent the areas in the MPL indicated in Fig. 2(b). The legend indicates the operating time.

operation at 0.60 A cm^{-2} are showed in Fig. 6(b) and (c). Fig. 6(b) shows that the amount of liquid water at locations 1 and 2 increased to 56 s of power generation and then oscillated at the same frequency. At location 3, the amount of water oscillated with opposite amplitude to the amount of water in locations 1 and 2 at a frequency of 3—6 s after an operating time of 81 s, indicating that location 3 periodically discharged its water and then was refilled

Fig. 6. Analysis of liquid water transport pathways and changes in the amount of liquid water at 0.60 A cm^{-2}. (a) The locations of areas used for calculation. Each square corresponds to an area of $35 \times 35 \, \mu m^2$. (b) Changes in the amount of liquid water at locations 1—6. (c) Changes in the amount of liquid water at locations 7—11 indicated in (a).

after its pressure reached the breakthrough pressure at 81 s. It is obvious that the locations 1, 2, and 3 are connected, as also can be observed in video clip 3. Next, we focus on location 3, 4, and 5. The amount of liquid water at location 3 decreased at almost the same time as the breakthrough at location 4 occurred, while it increased suddenly at location 5. This result suggests that the liquid water at locations 3 and 4 suddenly moved to location 5. However, the amount of liquid water at location 5 did not change much after its sudden increase, indicating that the pore at location 5 was almost full as a result of liquid water moving from locations 3 and 4. On the other hand, the amount of liquid water at location 6 suddenly increased at 90 s and oscillated with opposite amplitude to the amount of liquid water in locations 3, indicating that location 3 and 6 were connected. Therefore, location 3, 4, 5, and 6 are connected by the interconnected pores in the GDL. The oscillation in the amount of liquid water can be explained by the existence of a large pocket at location 3 that is connected with locations 5 and 6 by a smaller throat size. This observed liquid water transport is similar to the eruptive transport that was proposed to move the liquid water under the rib to the channel in the felt GDL [23]. Our observation clearly shows a pathway from the MPL to the GDL under the rib that could not be observed previously. This eruptive transport mechanism could be due to the non-uniform pore size in the liquid water transport pathway in the GDL. The pressure of the liquid water in the pocket must be higher than the capillary pressure in the vicinal throat in order to push the liquid water out of the pocket. The other three pathways show similar continuous liquid water transport, as indicated in Fig.6(c). The liquid water moved continuously without oscillation. From these results, we propose the liquid water pathways in the MPL and GDL shown in Fig. 7. The cracks in the MPL were connected with the pores in the GDL. The large pores in the GDL were connected with each other by smaller sized throats. We observed that the liquid water is transported in the same pathways at current density of 0.40 A cm^{-2} and 0.60 A cm^{-2}. This observation is in agreement with the proposals
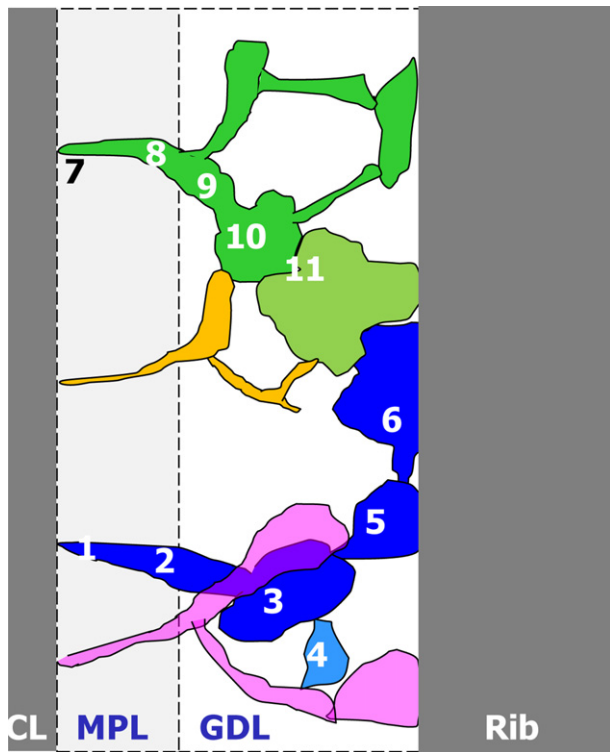
Fig. 7. Schematic picture of liquid water transport in the MPL and GDL observed in this study.

made by Gostick et al. [14] and Lu et al. [15] although they could not observe the pathways inside the MPL and GDL.

4. Conclusion

High-resolution soft X-ray radiography was used to investigate the dynamic water accumulation in the cathode MPL and GDL of an operating PEMFC. A water concentration gradient was observed in the MPL and GDL under the rib. The amount of liquid water accumulated in the MPL and GDL increased as the current density increased. The liquid water generated from the reaction was transported to the GDL mainly through the cracks in the MPL. The amount of liquid water in the MPL near the CL was low but became higher toward the GDL side. The dynamic liquid water transport in the cracks of the MPL and in the pores of the GDL was visualized. The interconnection between the cracks of the MPL and the pores of the GDL was observed.

Acknowledgments

References

[1] W. Dai, H. Wang, X.-Z. Yuan, J.J. Martin, D. Yang, J. Qiao, J. Ma, Int. J. Hydrogen Energy 34 (2009) 9461–9478.
[2] H. Li, Y. Tang, Z. Wang, Z. Shi, S. Wu, D. Song, J. Zhang, K. Fatih, J. Zhang, H. Wang, Z. Liu, R. Abouatallah, A. Mazza, J. Power Sources 178 (2008) 103–117.
[3] A. Bazylak, Int. J. Hydrogen Energy 34 (2009) 3845–3857.
[4] L. Cindrella, A.M. Kannan, J.F. Lin, K. Saminathan, Y. Ho, C.W. Lin, J. Wertz, J. Power Sources 194 (2009) 146–160.
[5] U. Pasaogullari, C.Y. Wang, K.S. Chen, J. Electrochem. Soc. 152 (2005) A1574–A1582.
[6] A.Z. Weber, J. Newman, J. Electrochem. Soc. 152 (2005) A677–A688.
[7] J.H. Nam, M. Kaviany, Int. J. Heat Mass Transfer 46 (2003) 4595–4611.
[8] R.P. Ramasamy, E.C. Kumbur, M.M. Mench, W. Liu, D. Moore, M. Murthy, Int. J. Hydrogen Energy 33 (2008) 3351–3367.
[9] D. Spernjak, A.K. Prasad, S.G. Advani, J. Power Sources 170 (2007) 334–344.
[10] S. Ge, C.Y. Wang, J. Electrochem. Soc. 154 (2007) B998–B1005.
[11] H.K. Atiyeh, K. Karan, B. Peppley, A. Phoenix, E. Halliop, J. Pharoah, J. Power Sources 170 (2007) 111–121.
[12] H. Nakajima, T. Konomi, T. Kitahara, J. Power Sources 171 (2007) 457–463.
[13] C.S. Kong, D.Y. Kim, H.K. Lee, Y.G. Shul, T.H. Lee, J. Power Sources 108 (2002) 185–191.
[14] J.T. Gostick, M.A. Ioannidis, M.W. Fowler, M.D. Pritzker, Electrochem. Commun. 11 (2009) 576–579.
[15] Z. Lu, M.M. Daino, C. Rath, S.G. Kandlikar, Int. J. Hydrogen Energy 35 (2010) 4222–4233.
[16] S. Tsushima, S. Hirai, Prog. Energy Combust. Sci. 37 (2011) 204–220.
[17] M.A. Hickner, N.P. Siegel, K.S. Chen, D.S. Hussey, D.L. Jacobson, M. Arif, J. Electrochem. Soc. 155 (2008) B427–B434.
[18] J. Fairweather, D. Spernjak, R. Mukundan, J. Spendelow, K. Artyushkova, P. Atanassova, D. Hussey, D. Jacobson, R.L. Borup, ECS Trans. 41 (2011) 337–348.
[19] J.S. Preston, U. Pasaogullari, D.S. Hussey, D.L. Jacobson, ECS Trans. 41 (2011) 319–328.
[20] K.T. Cho, M.M. Mench, Phys. Chem. Chem. Phys. 14 (2012) 4296–4302.
[21] A. Turhan, S. Kim, M. Hatzell, M.M. Mench, Electrochim. Acta 55 (2010) 2734–2745.
[22] P. Boillat, G. Frei, E.H. Lehmann, G.G. Scherer, A. Wokaun, Electrochem. Solid-State Lett. 13 (2010) B25–B27.
[23] I. Manke, Ch. Hartnig, M. Grunerbel, W. Lehnert, N. Kardjilov, A. Haibel, A. Hilger, J. Banhart, H. Riesemeier, Appl. Phys. Lett. 90 (2007) 174105.
[24] Ch. Hartnig, I. Manke, R. Kuhn, S. Kleinau, J. Goebbels, J. Banhart, J. Power Sources 188 (2009) 468–474.
[25] T. Mukaide, S. Mogi, J. Yamamoto, A. Morita, S. Koji, K. Takada, K. Uesugi, K. Kajiwara, T. Noma, J. Synchrotron. Radiat. 15 (2008) 329–334.
[26] H. Markötter, I. Manke, Ph. Krüger, T. Arlt, J. Haussmann, M. Klages, H. Riesemeier, Ch. Hartnig, J. Scholta, J. Banhart, Electrochem. Commun. 13 (2011) 1001–1004.
[27] T. Sasabe, S. Tsushima, S. Hirai, Int. J. Hydrogen Energy 35 (2010) 11119–11128.
[28] T. Sasabe, P. Deevanhxay, S. Tsushima, S. Hirai, J. Power Sources 196 (2011) 8197–8206.
[29] P. Deevanhxay, T. Sasabe, S. Tsushima, S. Hirai, Int. J. Hydrogen Energy 36 (2011) 10901–10907.
[30] T. Sasabe, P. Deevanhxay, S. Tsushima, S. Hirai, Electrochem. Commun. 13 (2011) 638–641.
[31] P. Deevanhxay, T. Sasabe, S. Tsushima, S. Hirai, Electrochem. Commun. 22 (2012) 33–36.
[32] T. Kitahara, T. Konomi, H. Nakajima, Y. Tateishi, Trans. Jpn. Soc. Mech. Eng. 74 (2008) 2221–2228.
[33] Z. Fishman, A. Bazylak, J. Electrochem. Soc. 158 (2011) B846–B851.